J Mol Model (2012) 18:2869–2883
DOI 10.1007/s00894-011-1308-9

ORIGINAL PAPER

Global and local molecular dynamics of a bacterial carboxylesterase provide insight into its catalytic mechanism

Xiaozhen Yu · Sara C. Sigler · Delwar Hossain · Monika Wierdl · Steven R. Gwaltney · Philip M. Potter · Randy M. Wadkins

Received: 25 July 2011 / Accepted: 8 November 2011 / Published online: 30 November 2011

Abstract Carboxylesterases (CEs) are ubiquitous enzymes responsible for the detoxification of xenobiotics. In humans, substrates for these enzymes are far-ranging, and include the street drug heroin and the anticancer agent irinotecan. Hence, their ability to bind and metabolize substrates is of broad interest to biomedical science. In this study, we focused our attention on dynamic motions of a CE from *B. subtilis* (pnbCE), with emphasis on the question of what individual domains of the enzyme might contribute to its catalytic activity. We used a 10 ns all-atom molecular dynamics simulation, normal mode calculations, and enzyme kinetics to understand catalytic consequences of structural changes within this enzyme. Our results shed light on how molecular motions are coupled with catalysis. During molecular dynamics, we observed a distinct C-C bond rotation between two conformations of Glu310. Such a bond rotation would alternately facilitate and impede protonation of the active site His399 and act as a mechanism by which the enzyme alternates between its active and inactive conformation. Our normal mode results demonstrate that the distinct low-frequency motions of two loops in pnbCE, coil_5 and coil_21, are important in substrate conversion and seal the active site. Mutant CEs lacking these external loops show significantly reduced rates of substrate conversion, suggesting this sealing motion prevents escape of substrate. Overall, the results of our studies give new insight into the structure-function relationship of CEs and have implications for the entire family of α/β fold family of hydrolases, of which this CE is a member.

Keywords Dynamics · Enzyme kinetics · Esterase · Normal mode · Substrate specificity

Abbreviations

CE	carboxylesterase
CPT-11	irinotecan, 7-ethyl-10-[4-(1-piperidino)-1-piperidino]carbonyloxycamptothecin
hiCE	human intestine carboxylesterase
hCE1	human carboxylesterase 1
pnbCE	*p*-nitrobenzyl esterase
rCE	rabbit carboxylesterase
MD	molecular dynamics
AChE	acetylcholinesterase
DCCM	dynamic cross-correlation map
SN-38	7-Ethyl-10-hydroxy-camptothecin
NMA	normal mode analysis
o-NPA	ortho-nitrophenyl acetate
mAChE	mouse acetylcholinesterase
RMSD	root-mean-square deviation
RTB	rotation-translation-block
PDB	protein data bank
MMTK	molecular modeling toolkit

Electronic supplementary material The online version of this article (doi:10.1007/s00894-011-1308-9) contains supplementary material, which is available to authorized users.

X. Yu · S. C. Sigler · R. M. Wadkins (✉)
Department of Chemistry & Biochemistry,
University of Mississippi,
University, MS 38677, USA
e-mail: rwadkins@olemiss.edu

M. Wierdl · P. M. Potter
Department of Chemical Biology and Therapeutics,
St Jude Children's Research Hospital,
Memphis, TN 38105, USA

D. Hossain · S. R. Gwaltney
Department of Chemistry and Center for Environmental Health Sciences, Mississippi State University,
Mississippi State, MS 39762, USA

Introduction

Carboxylesterases (CEs) are ubiquitous enzymes responsible for the detoxification of xenobiotics. They are found in organisms ranging from bacteria to man [1, 2]. In humans, therapeutically-useful drugs are metabolized by these enzymes, which impacts upon the efficiency of some drug treatments [3]. For example, CEs convert inactive prodrugs to active metabolites, a process that is essential for the biological activity of drugs such as the anticancer agents CPT-11 and capecitabine, the antibiotics Ceftin and Vantin, as well as the illicit street drug heroin. However, more commonly, CEs hydrolyze many esterified drugs to inactive products that are then excreted. Agents such as flestolol, meperidine, lidocaine and cocaine, are all hydrolyzed and inactivated by these enzymes. Therefore the efficacy of esterified drugs will be dependent upon the distribution and catalytic activity of different CEs.

Both CE substrates and inhibitors of CEs show selectivity among isoforms from different species, despite the overall structural homology of the enzymes. Examples are given in references [4–10], where selected inhibition of two human enzymes (hiCE and hCE1) can be accomplished, depending on the structure of the inhibitor. Similar selectivity in the substrates for these enzymes has also been noted [11].

The specificity of CEs for a particular substrate or inhibitor depends on the enzyme's molecular structure, and importantly, on the dynamics of conformational substructures present within an enzyme when a substrate is bound (i.e., "conformational sampling" [12]). Structural dynamics of CEs, therefore, have critical roles in drug detoxification and can be studied by a combination of experimental and theoretical techniques. Once a fundamental understanding of the relationship between enzyme dynamics and substrate selectivity is established, modulation of CE activity by mutation of known enzymes may allow for improvements in, and potentiation of, substrate conversion [13]. Such mutants might, for example, be used as a therapeutic agent for treatment of heroin overdoses or for exposure to nerve agents such as sarin.

Studying the substrate and inhibitor selectivity of a CE from *B. subtilis* has proven it to be an interesting model system for understanding the contribution of enzyme dynamics to the substrate catalysis. The *p*-nitrobenzyl esterase (pnbCE) from this bacterium has a structural homology that is similar to the CE found in rabbit liver (rCE) [14]. Further, its crystal structure has been determined [15], allowing for the 3-dimensional localization of specific residues. Its cloning and expression has made for a simple system to characterize at the molecular level the contribution of specific amino acid residues to both substrate selectivity and the effect of inhibitors. For example, an exploration of the "side door" hypothesis for substrate release by pnbCE has been recently performed, where the kinetics of substrate turnover are shown to be highly dependent on the L362 residue located at the bottom of the active site gorge [16].

However, to truly understand the individual residue contributions to the catalytic properties of an enzyme, molecular dynamics (MD) need to be taken into account. The use of MD in the development of enzyme inhibitors for the related α/β hydrolase acetylcholinesterase (AChE) has been recently reviewed [17] and these principles also apply to CEs. Briefly, enzymes are in constant motion at temperatures near 37 °C and the understanding of the fluctuation is crucial for understanding of the interactions of the enzyme with its substrate or inhibitors. In the α/β fold hydrolase family, the active site residues are at the bottom of a ~22 Å gorge, the walls of which are also fluctuating. This is especially important given that, in the pnbCE crystal structure, the active site gorge is too small to accommodate large substrates like CPT-11. However, the large CPT-11 molecule is indeed a substrate for pnbCE [14]. This dilemma can be resolved by structural fluctuations at both the active site opening as well as within the gorge. Taking fluctuations into consideration is particularly useful to understanding how substrates and inhibitors bind to the active site, and such knowledge may, in turn, lead to successful design of enzyme inhibitors [18].

Acetylcholinesterase has been the subject of considerable MD simulation for the reasons given above (reviewed in [17, 19]). In contrast, only a few studies of the MD of CEs have been reported [16, 20, 21]. Among them, a short 400 ps simulation of wild type pnbCE was compared with two thermostable mutants [20]. These authors noted that the thermostable mutants showed increased populations of low-frequency vibrational modes and suggested that this reflected concerted motions that provided stability to the native state versus the denatured state. However, the connection between these low-frequency motions and catalytic efficiency was not explored. It has become clear in recent years that dynamics have a profound influence on the catalytic properties of enzymes [12, 22, 23]. In this report, we have examined both the low-frequency and high-frequency motions of pnbCE, with emphasis on the question of what individual domains of the enzyme might contribute to the catalytic activity. We have used both a long 10-ns all-atom MD simulation with AMBER 8 [24] as well as normal mode calculations (ElNémo; [25]) to determine the largest structural changes within the pnbCE. Our results describe both distinct low-frequency and high-frequency motions that involve residues near the active site and the putative "side door" Leu362 that control entry of substrate and exit of hydrolyzed product. Since pnbCE is a bacterial enzyme, it can be easily modified, expressed, and purified using *E. coli*. After identification of dynamic

motions in two large loops near the active site entrance via computational methods, we generated mutant enzymes with these loops deleted to assess the effects of such mutations on catalysis. The roles of the surface dynamic loops gating the active site of different enzymes have been studied via various computational analyses [26–28]. However, evidence to support these proposed mechanisms are still very limited, especially for carboxylesterases. Below, we detail our findings and comment on the overall role molecular dynamics play in the catalytic mechanisms of CEs.

Methods and materials

pnbCE structure

The structure of *B. subtilis* carboxylesterase (pnbCE) was taken from Protein Data Bank entry 1QE3 [15]. Two loops, residues 66–74 and 414–420, are missing from the crystal structure and were inserted using Modeller [29]. The resulting structure was then minimized with respect to energy using the *sander* module of AMBER 8 [30]. The secondary structure assignment of pnbCE was done by program STRIDE (a knowledge-based pattern recognition algorithm used for protein secondary structure assignment) [31]. Like other carboxylesterses, pnbCE is folded into three domains, a catalytic domain, an α/β domain and a regulatory domain. A total of 15 α-helices, 14 β-sheets, and 25 coils and turns were assigned by the program (see Fig. 1).

Molecular dynamics simulations

MD simulations were performed with the AMBER 8 software suite using the ff94 force field [32] and the pairwise generalized Born model [33]. Energy was minimized for 100 cycles of 2 fs and followed by a 10 ps equilibration cycle, with positional restraints on all atoms. Temperature of the system was gradually increased from 0 K to 300 K during the equilibration process. The MD simulation then used a cutoff of 12 Å for non-bonded interactions and weak-coupling algorithm [34] was used to maintain a 300 K constant temperature. A total of 10 ns of MD simulation was performed using a 2-fs time step in conjunction with the SHAKE algorithm [35] to constrain bond length between hydrogen and heavy atoms in the system. All the simulations were conducted on the Mississippi Center for Supercomputing Research's Altix cluster computer.

Analysis of the MD data was done on a dual-core Mac desktop. First, the total energy of the 10-ns MD simulation was plotted with respect to time to determine the regime within which the MD reflects statistical equilibrium fluctuations around the energy minimum. Then the *ptraj* program from AMBER was used to calculate the root mean-square fluctuation (RMSD) of four residues: active site Ser189, Glu310, His399 and "side door" Leu362, with respect to their starting coordinates.

An in-house python program using the molecular modeling toolkit (MMTK) module [36], was used to analyze the MD simulation trajectory. The analysis was

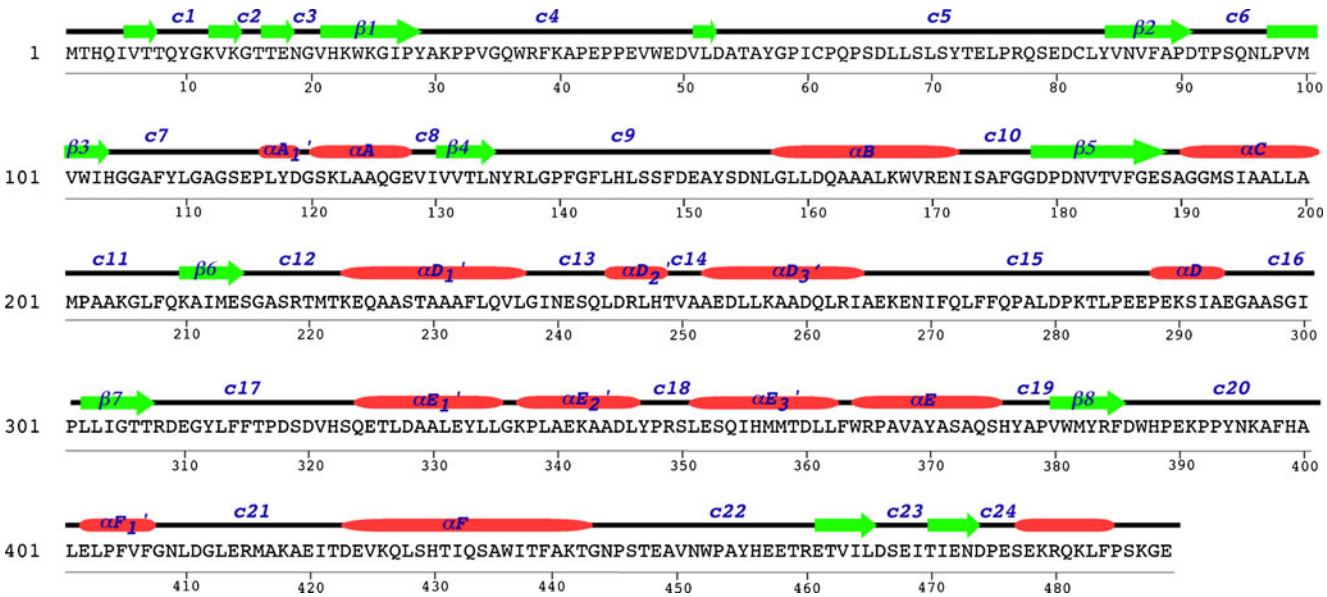

Fig. 1 The sequence and secondary structural assignment of pnbCE. The secondary structures of pnbCE are illustrated with different color diagrams: green arrows are β-sheets (β1- β8), red bars are helices (αA-αF) and coils/turns in between (c1-c24). The naming scheme is chosen to be consistent within the α/β fold hydrolase family [48]. The α/β fold helices are labeled as αA, αB, αC, αD, αE and αF. The helices in the excursions are primed (') and labeled as αA_1' before αA; αD_1', αD_2', αD_3' before αD; αE_1', αE_2', αE_3' before αE and αF_1' before αF

performed with a procedure modified from the work of McCammon and colleagues [37]. As active site Ser189 and His399 are the two residues proposed to make initial contact with the ester bond to be cleaved (Fig. 2) [1], the molecular surface of pnbCE was calculated at each step of the dynamics using a probe radius that was incremented by 0.1 Å until active site Ser189 and/or His399 no longer contributed to the molecular surface. The largest probe radius that could contact both residues was considered to provide the diameter of the active site gorge. The gorge diameter is plotted with respect to time in Fig. 3b.

The docking of p-NPV into the pnbCE structure was done using AutoDock 3 [38]. A model of p-NPV with HF/6-31 G* ESP charges was docked into an annealed pnbCE structure. The resulting structure was simulated as above, with the exception of using the ff99 force field [39] and its accompanying GAFF force field [40] for the p-NPV. One ns of MD simulation was run for the complex. An MM-GBSA [41] pairwise decomposition for the binding enthalpy of the p-NPV to the pnbCE was performed on the MD trajectory, and the results were analyzed by coil. Many of the residues in coil_7 showed significant interactions with p-NPV, while none in coil_5 or coil_21 did.

Normal mode analysis

Normal mode analysis (NMA) was performed on the ElNémo web server [25], which is a web interface to the Elastic Network Model that implements the 'rotation-translation-block' (RTB) approximation. RTB approximation groups several residues into a super-residue based on the number of residues in the protein. The minimized starting structure was used as the input PDB file. The number of residues that are treated as a rigid body value (NRBL) was determined by the server as a function of protein size to optimize computation speed. A cutoff of 8 Å was used to identify elastic interactions. The first six zero-frequency modes contain the overall rotations and translations of the system. Our focus was the 5 lowest non-zero frequency modes (modes 7–11) that were generated. The output of NMA is a series of trajectory files in Protein Data Bank (PDB) format, which include 11 structures by default: the original input structure and ten frames representing the motions between the two conformational extrema of the normal mode.

Modes 8, 9 and 10 have a low degree-of-collectivity value around 0.1, which meant only a few atoms were

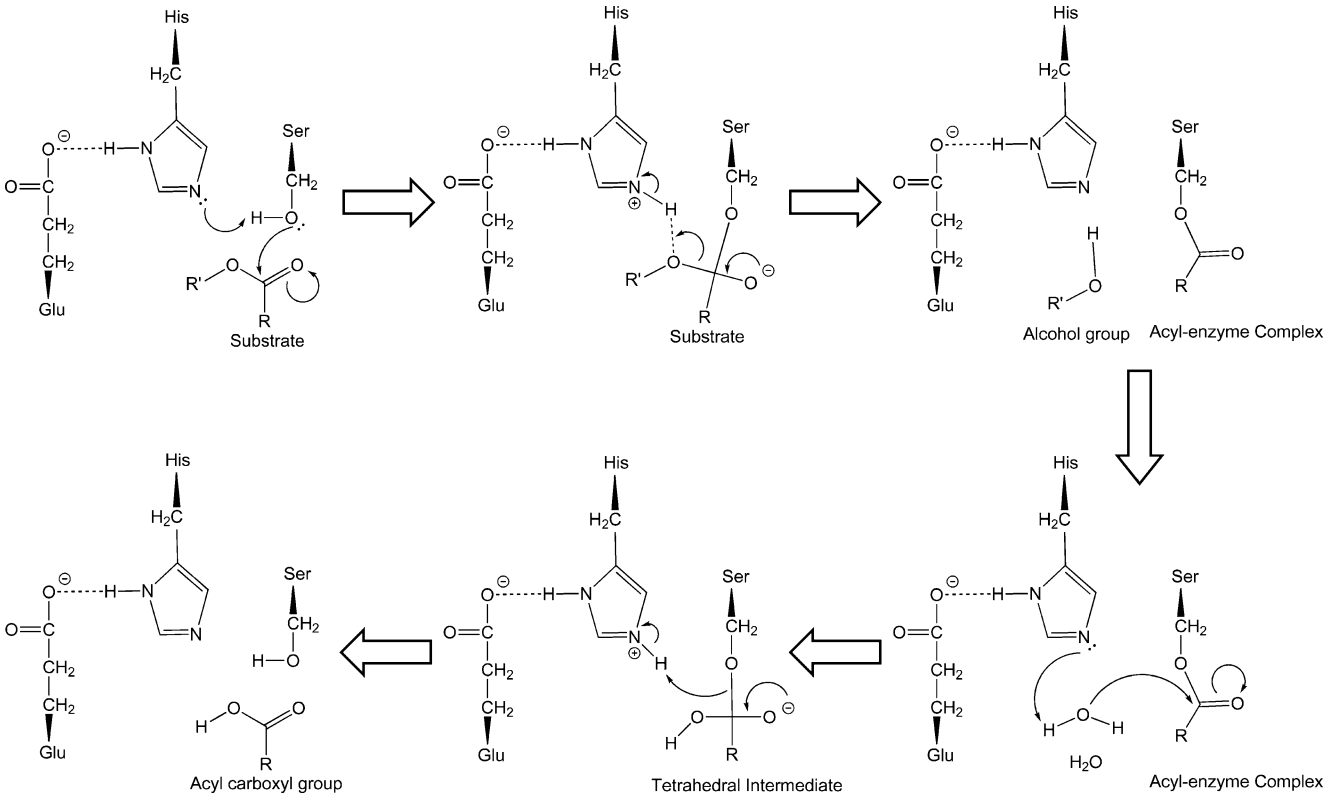

Fig. 2 Proposed catalytic mechanism of hydrolysis catalyzed by CEs. Hydrogen bonding between the Glu310 and His399 increases the basicity of the histidine $N_{\varepsilon 2}$ allowing it to initiate a nucleophilic attack during hydrolysis. In the subsequent step, the proton is removed from the now-acidic histidine. The conformational changes in Fig. 6 provide a physical mechanism for how this residue can alternate between basic and acidic forms

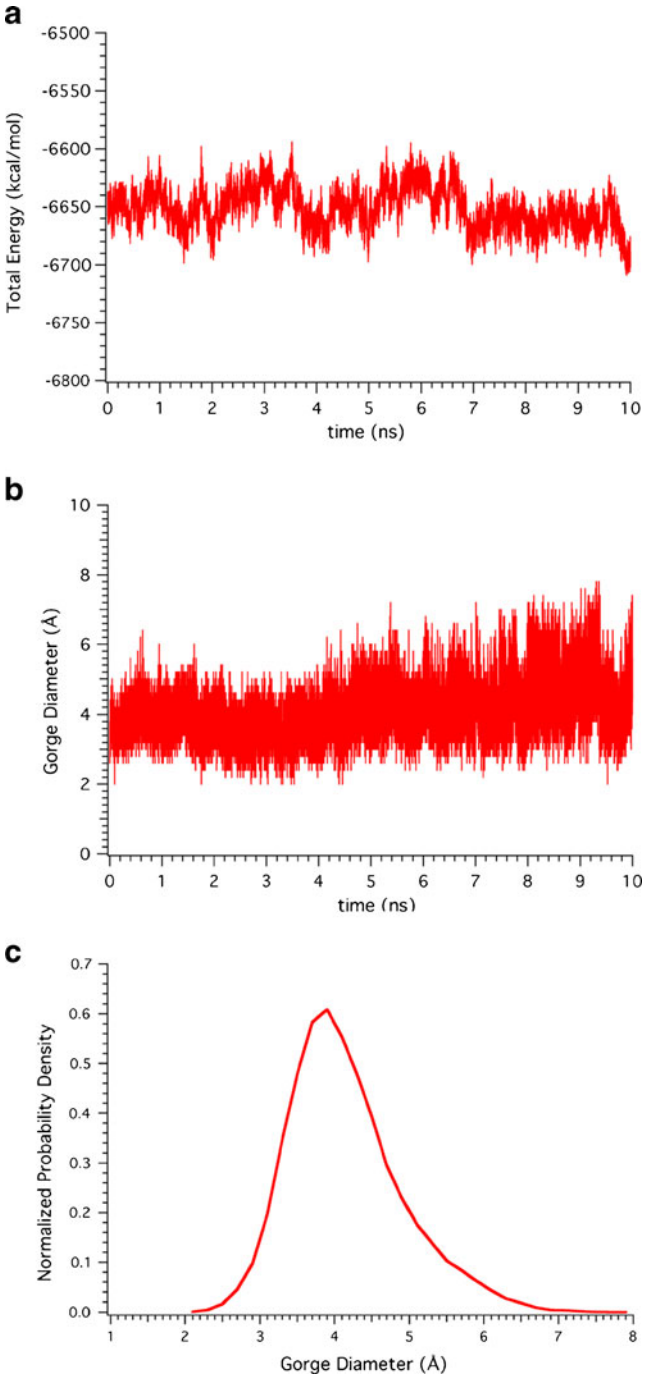

Fig. 3 MD simulation of pnbCE (**a**) Total energy fluctuation in kcal mol^{-1} during 10-ns MD simulation is presented, indicating equilibrium sampling during the trajectory. (**b**) The pnbCE active site gorge diameter during 10-ns MD simulation. The diameter of active site gorge fluctuates between 2 Å to 7 Å and increases its fluctuation with time during the 10-ns MD simulation. (**c**) The normalized probability density distribution of pnbCE gorge diameter

involved in these motions. Additionally, the motions were all localized within the N- or C-terminus of the structure. For the purpose of analyzing structural and functional relationship, these modes were ignored due to the lack of global conformational significance. Meanwhile, modes 7 and 11 had high degree-of-collectivity values of 0.24 and 0.34, respectively. These two modes were used for further analysis.

The mean square displacement $<R^2>$ of all C-α atoms in mode 7 was calculated from comparison with the input structure. By using the relationship $B=(8\pi^2/3)\ <R^2>$, predicted B-factors were calculated for both mode 7 and 11[42]. Both $<R^2>$ and predicted B-factors are arbitrary numbers, and can be linearly scaled for comparison purpose. The experimentally observed B-factor was obtained from the x-ray crystal structure of pnbCE. In Fig. 4, both predicted B-factors were scaled and plotted with the actual B-factor, providing a measure of how well the protein's fluctuation in the crystal structure was represented by these two low-frequency normal modes. The Pearson product–moment correlation coefficient (Pearson r) between the predicted and actual B-factors is calculated by the Prism software.

Cross-correlation analysis was performed on all the residue pairs in pnbCE for mode 7 and 11, respectively. The cross-correlation coefficient C_{ij}, between atoms i and j, was computed as Eq. 1:

$$c_{ij} = \frac{\langle \overline{R}_i \bullet \overline{R}_j \rangle}{\sqrt{\langle \overline{R}_i^2 \rangle \bullet \langle \overline{R}_j^2 \rangle}}, \tag{1}$$

where R_i and R_j are the displacement vectors for atom i and j, respectively and the brackets indicate an average over the trajectory. The value of c_{ij} was calculated using an in-

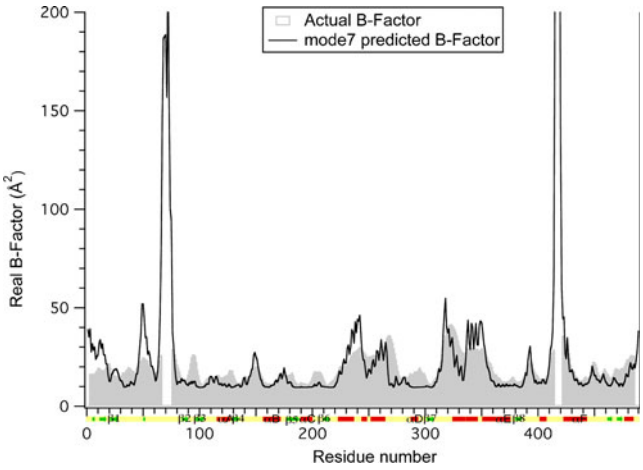

Fig. 4 The experimental and predicted B-factors of pnbCE. The solid gray area is the experimental B-factor taken from its crystal structure (PDB entry 1QE3). Solid lines are the predicted B-factors from analysis of normal mode 7. Predicted B-factors are scaled for comparison purpose. The colored bar under the abscissa is used to represent the secondary structure assignment: green arrows are ß-sheets, red regions are helices and yellow regions are coils and turns. The signature α/β fold hydrolase regions are indicated by αA-αF and β1-β8

house python program. Input of the program is the trajectory file (in PDB format) that was generated by ElNémo server. The result was loaded into a 489 x 489 matrix and the value of c_{ij} ranged from −1.0 (fully anti-correlated, residue pair moving in the opposite direction) to 1.0 (fully correlated, residue pair moving in the same direction). In Fig. 5, only the top 20% of the correlated motions are shown in these dynamic cross-correlation maps (DCCM).

Active site pocket identification and measurements were done on CASTp server [43]. The weighted Delaunay triangulation and the alpha complex are used for shape measurements [44]. The calculation used default atomic radii and a solvent probe of radius 1.4 Å. Measurements for both solvent accessible surface (Lee-Richards' surface [45]) and molecular surface (Connolly's surface [46]) were calculated by the server.

Bacterial strains, vectors, gene isolation and mutagenesis

The host bacterial strain for plasmid preparation, XL-10 gold supercompetent cells, were purchased from Stratagene. The E. *coli* expression host strain, *Origami B(DE3) pLacI* and the expression vector pTriEx-3, were obtained from Novagen. The pnbA gene encoding pnbCE was isolated from *B. subtilis* genomic DNA using PCR as described earlier [14]. The pnbA coding sequence was inserted into the BamHI restriction site of pTriEx-3 vector, to create the pTriEx-3/pnbA plasmid DNA.

Both mutant enzymes were generated by using the Phusion site-directed mutagenesis kit from Finnzymes. Using pTriEx-3/pnbA plasmid as a template, the Δ[coil_5] pnbCE mutant was made by PCR using primer pair: 5′-(phosphate) CGCCAGTCCGAGGATTGCTTG -3′ and 5′-(phosphate) AGACGGCTGCGGGCAAATAGAG. The Δ[coil_21] pnbCE mutant was made using primer pair: 5′-(phosphate) ATTACGGATG AGGTGAAACA GCTTTCTC -3′ and 5′-(phosphate) CAATCCGTCC AGATTTCCAA AGAC -3′. Linear PCR products were purified using QIAquick PCR purification kit (QIAGEN), and were ligated back into circular plasmid DNA. After transformed to XL-10 Gold super-competent cells, both deletion mutants plasmid were purified using QIAfilter plasmid purification kit (QIAGEN). All three deletion mutants were confirmed by DNA sequencing. The purified mutants, along with the wild-type (wt-) pnbCE showed nearly identical circular dichroism (CD) spectra and melting temperatures, and our data agreed with prior studies of related enzymes [47], indicating the mutations did not change the overall folding of pnbCEs.

Protein expression and purification

Both deletion mutants, along with wt-pnbCE plasmids were transformed into the Origami B cells. After bacterial growth, protein expression was induced with 1 mM IPTG for 3 ~ 4 hours. Cells were harvested with centrifugation and protein extracted using 30 mL of Bug-Buster reagent (Novagen). Protein extracts were dialyzed against 10 mM

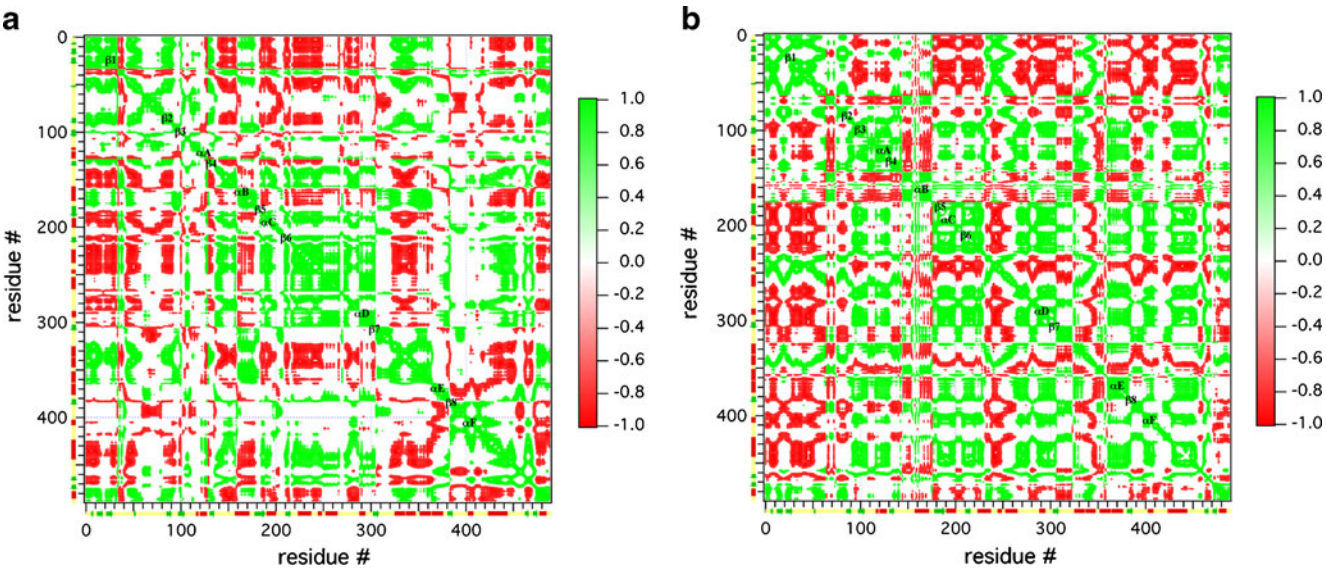

Fig. 5 Dynamic cross-correlation maps from normal mode analysis. These plots show correlated motions of the C_α atoms between all residue pairs in (**a**) mode 7, and (**b**) mode 11. The green-red scale color bar on the right indicates the extent of the correlation. Green indicates a high level of correlated motions (residue pairs move together in the same direction), while red indicates anti-correlated motions (residue pairs move together in the opposite direction). To highlight the collective motions, only motions in the top 20% of the color scale (−1.0 to −0.8 and 0.8 to 1.0) are shown

HEPES buffer (pH 7.4) overnight before proceeding to isoelectric focusing. The wt-pnbCE and Δ[coil_21] pnbCE mutant CEs were mixed with Bio-Lyte 3/5 ampholytes (Bio-Rad), while Δ[coil_5] pnbCE mutant was mixed with Bio-Lyte 5/7 ampholytes. After 4∼5 hours of focusing, 20 protein fractions were collected. CE activity was tested and the fractions with high levels of CE activity were pooled. Salt concentration was adjusted to 1 M using 4 M NaCl. The ampholytes were removed by overnight dialysis in 10 mM Hepes (pH 7.4) with 50 mM NaCl. The molecular weight of each protein was determined by applying a protein sample to a calibrated Superose 12 10/300 chromatography column (GE Healthcare). Protein concentrations were determined by standard Bradford protein assay and purity assessed by polyacrylamide gel electrophoresis. The purified enzymes were used in the circular dichroism spectroscopy and enzymatic kinetic assays.

Circular dichroism spectroscopy

CD spectra for all three enzymes were acquired on a Model 202SF CD Spectrometer (Aviv) from 200 to 300 nm, with a 5 s averaging time in 5 mM sodium phosphate, 50 mM NaCl, pH 7.4. The measured delta absorbance is converted into the mean residue ellipticity unit (degrees·cm^2·dmol^{-1}·residue^{-1}). In the supplemental Fig. 1, it is shown that CD spectra of the wild-type and mutant pnbCEs are similar, indicating the mutations did not change the overall folding of pnbCEs.

For the temperature-induced unfolding experiment, a 1-cm cuvette with a screw top was used to prevent evaporation of the solution at high temperatures. The temperature probe was inserted through the cuvette screw top to monitor temperature changes. Protein concentrations of 1 μM in 5 mM sodium phosphate, 50 mM NaCl, pH 7.4, were used for denaturation experiment. The unfolding measurement was performed within a temperature range of 15–85 °C. The temperature ramp was set at 1 °C/min, with data taken every degree. The equilibration time at each temperature was 30 s. The acquisition time was 5 s. The measurements were taken at 222 nm. The melting temperature (T_m) is calculated based on the curve fitting of the data points. As indicated in supplemental Fig. 1b, the T_m of wt-pnbCE is 57.25 °C, which matches the literature value [47]. The two mutants unfold at 51.04 °C for Δ[coil_5] pnbCE and 54.45 °C for Δ[coil_21] pnbCE, indicating they are fully folded at the kinetics assay temperature of 25 °C.

o-NPA kinetics

Kinetic parameters were determined by incubating different concentrations of o-NPA with constant amounts of CEs. o-NPA solutions were diluted into ranges from 16 mM to 0.25 mM in 50 mM HEPES buffer (pH 7.4) with a 16 mM o-NPA stock. The conversion of o-NPA to o-NP was monitored at 420 nm for 30 s. The reaction velocities were calculated from the data points and the kinetic parameters and r^2 values are determined by using non-linear regression with Prism software (Graph Pad).

Results

Overall description of pnbCE

The enzyme is an α/β fold hydrolase consisting of 489 amino acids and is folded into three domains: a regulatory domain, an α/β domain and a catalytic domain [15]. The regulatory domain is comprised of helices αF and the c-terminal helix (see Fig. 1 for secondary structure designation). The naming scheme in Fig. 1 is chosen to be consistent within the α/β fold hydrolase family [48]. Between the regulatory domain and the catalytic domain lies the α/β domain, which is composed of five α-helices (αA-αE) and eight β-sheets (β1-β8) adjacent to each other. The α/β fold which carries the catalytic machinery is the best-conserved structural features in the α/β fold hydrolase family. Besides the α/β fold helices and β-sheets, there are some excursions of varying length that occur in each member of the family (indicated by primes (') in Fig. 1). Within the catalytic domain, three highly conserved active site residues (Ser189, Glu310 and His399) are located at the bottom of a ~22 Å by ~13 Å by ~18 Å cavity, which is similar to all other known CEs [3]. In the crystal structure of pnbCE, the diameter of the active site gorge is ~3.6 Å wide, which would only accommodate small substrates in specific orientations. From the static crystal structure of pnbCE there is no clear way to understand how a large substrate like CPT-11 could be positioned into the gorge for hydrolysis. Both molecular dynamic simulation and normal mode analysis were used to explore, among other things, the flexibility of the gorge and its impact on substrate selectivity. Similar to the human liver CE (hCE1) structure, the flexibility and chemical environment of the gorge allows pnbCE to act on structurally distinct compounds [49].

Molecular dynamics simulations

Molecular dynamics (MD) simulation is a principal tool in the study of biological molecules. It has been primarily used in examining high-frequency motions of protein on the ps to ns time scale using force calculations of greater accuracy and complexity (e.g., the AMBER force field). After energy minimization and equilibration of the complete pnbCE molecule, a 15 ns MD simulation was performed. During the simulation process, the pnbCE molecule reached its local energy minimum after ~5 ns and fluctuated around −6651.37±16.94 (mean±sd) kcal mol^{-1} (Fig. 3a), indicating

that our model provided a reasonable starting structure for our simulation, and the remaining 10 ns was used as the time window for the analysis below.

Figure 3b & c illustrates the gorge diameter fluctuations of pnbCE from our MD simulation, which is a measure of the largest substrate that can reach the catalytic active site triad. Overall, the average gorge diameter fluctuated at 4.05± 0.45 Å throughout the simulation. However, the diameter size collapsed to 2.0 Å at its narrowest to as large as 7.8 Å at its widest. The size and fluctuation of the gorge diameter increased during the simulation, from 3.81±0.48 Å (first 2 ns) to 4.71±0.85 Å (last 2 ns). These diameters are significantly larger than that reported for the related enzyme acetylcholinesterase (AChE) [19], where the gorge diameter fluctuations were found to be 3.04±0.52 Å. Further, we do not see the bimodal switch in gorge diameter that was observed for AChE and that has been postulated to act as a gating mechanism during the hydrolysis of AChE substrates (Fig. 3c). As we have noted earlier, CPT-11 has a conical molecular volume, with the wider end having a diameter of 7.8 Å and the narrower end a diameter of 3.1 Å [11]. The gorge fluctuations shown in Fig. 3b indicate that pnbCE could accommodate a molecule the size of CPT-11 with little difficulty.

Active site and "side door" residues

The catalytic triad, Ser189, Glu310 and His399, is highly conserved among CEs [50]. As noted in Fig. 2, it is proposed that hydrolysis is initiated by nucleophilic attack of the β-OH group of Ser189 on the carbonyl group of the substrate [51]. According to this theory, a low-barrier hydrogen bond between Glu310 and His399 facilitates the initial nucleophilic attack by Ser189 and stabilizes the tetrahedral intermediate. Therefore, the conformational change involving this Glu-His hydrogen bond is essential for the hydrolysis mechanism. The root mean square deviation (RMSD) of the active site and "side door" residues from MD simulation revealed detailed features of the active site residue Glu310 and the "side door" residue Leu362. Both residues alternate between two distinctive conformations during the whole of the dynamic simulation. These two conformations are characterized by two distinct RMSD values (vs. the crystal structure); Glu310 fluctuates between positions that are 1.3 Å and 1.5 Å RMSD while Leu362 fluctuates between positions that are 0.7 Å and 2.1 Å RMSD. This is illustrated in Fig. 6a by focusing on the 1.0 ns region between 6.0 ns to 7.0 ns of the MD simulation. The conformational details are given in a snapshot at 6.5 ns that shows both Glu310 and Leu362 at their high-RMSD conformation, and another snapshot at 6.8 ns that shows their low-RMSD conformation (Fig. 6b). The two conformations are colored with green and blue to indicate the changes observed.

The large RMSD changes in Fig. 6a are caused by bond rotation in the two conformations. In moving between the two conformations, the C-C bond of Glu310 rotates 120° from an inactive conformation (blue structure in Fig. 6b) where the hydrogen bond is not made into an active conformation (green structure in Fig. 6b) where it is made. As shown in Fig. 6b, one of the oxygen atoms ($O_{\varepsilon 1}$) on Glu310 is highlighted in red. In the active conformation (green structure), a hydrogen bond is clearly established between this oxygen atom and the hydrogen on His399. As the side chain of Glu310 rotates 120° around its C-C bond, this hydrogen bond is broken and the active site turns into its inactive conformation (blue structure).

Also on this time scale, Leu362 rotates 180° around its C-C bond and adopts two distinct conformations, one of which moves the side chain of the Leu362 away from the active site residue Ser189 by an additional 1.5 Å. This conformational change would make it possible for small hydrolysis products to be released from the enzyme via this "side door". Although speculative, such a rotation as part of the catalytic cycle might also explain the catalytic effects observed in mutation studies of the Leu362 residue [14]. Mutation of the Leu residue to Lys and Arg would introduce a long, bulky side chain to the residue that would constrain rotational motions and potentially block product from exiting this "side door". This would be especially true for large products, which would help to explain why the substitution of Leu with Arg or Lys inhibits CPT-11 metabolism 10- or 5- fold, respectively, but has modest effects on o-NPA catalysis.

Normal mode calculations

Although MD simulation is widely used for studying the motions of biomolecules, normal mode analysis (NMA) provides an important alternative to MD simulation because it is much less demanding in terms of CPU time and is able to provide information about low-frequency motions that usually reflect global structural changes of biomolecules on a residue-by-residue basis [52]. While NMA allows us to explore the lowest-frequency motions in pnbCE, given the simple empirical energy function used to analyze the motions, no timescale is available for the resulting motions (i.e., the simplified force constants used in NMA are not the true force constants acting on the atoms). Similar loop motions in other enzymes are on the micro- to millisecond time scale are correlated with the catalytic cycle [22] and those observed during NMA most likely are on this time scale as well.

The first five lowest-frequency vibrational normal modes for pnbCE were generated by the ElNémo web server [25]. Two of these five modes (mode 7 and 11) with higher degrees of collectivity were used for further analysis since they represented two major global motions. To compare

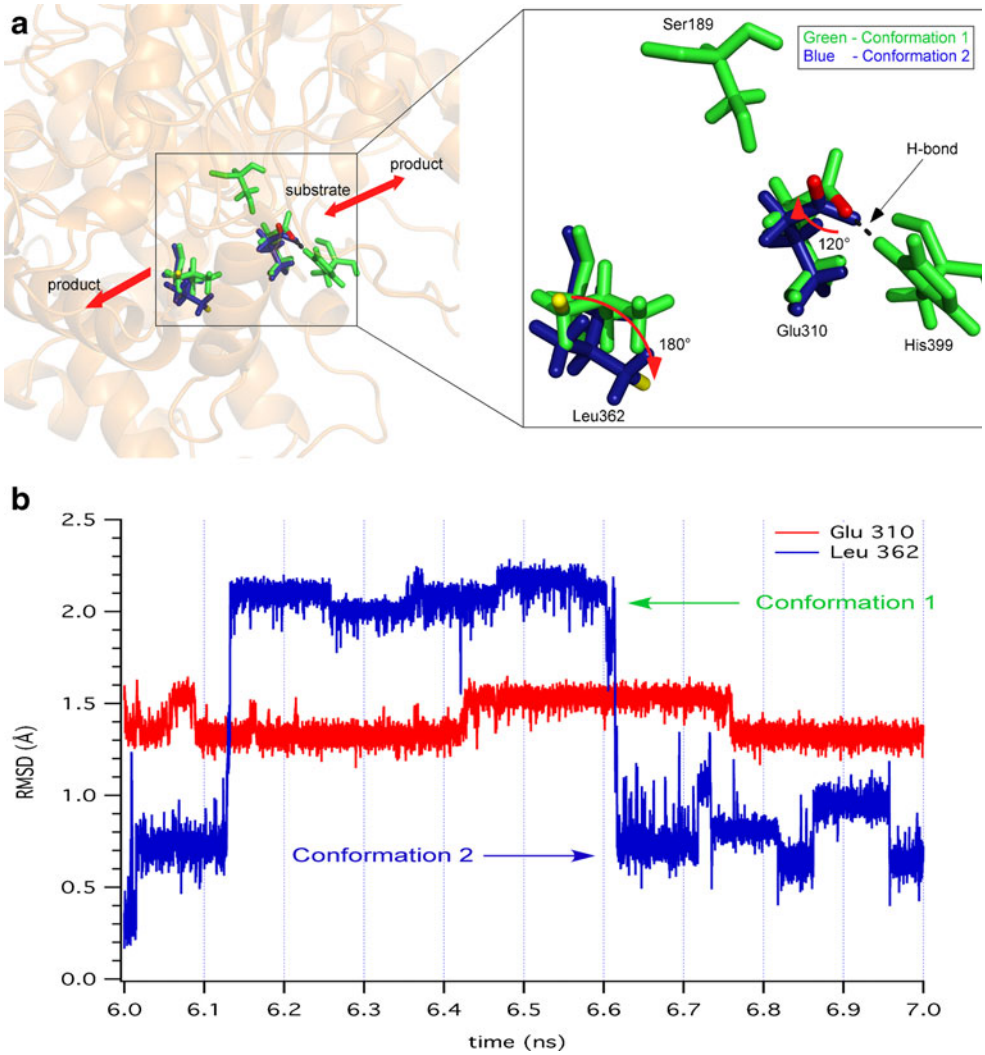

Fig. 6 The conformational changes of two residues Glu310 and Leu362. (**a**) The RMSD of two residues Glu310 and Leu362 with respect to their initial coordinates as a function of time for pnbCE. As part of the catalytic triad, Glu310 alternates between two conformations around 1.5 Å RMSD. Meanwhile, the "side door" residue Leu362 also alternates between two major conformations. Both conformation 1 (green) and 2 (blue), as indicated by arrows, correspond to the same two conformations in Fig. 6b. (**b**) A snapshot of pnbCE from the MD simulation showing the active site Glu310 and "side door" residue Leu362 in their two conformations (Fig. 6a). The transparent cartoon representation in the background is the backbone of pnbCE and red arrows indicate the possible directions of substrate and product movement. The catalytic triad (Ser189, Glu310 and His399) and "side door" (Leu362) from two conformations are highlighted in blue (6.5 ns point in Fig. 6a) and green (6.8 ns point in Fig. 6a). The same oxygen atom ($O_{\varepsilon 1}$) on Glu310 and hydrogen atom ($1H_{\delta 1}$) on Leu362 in two conformations are highlighted in red and yellow, respectively. Red solid arrows are used to indicate the bond rotations that occur during the conformational change

with experimental data, the mean square displacement$<R^2>$of the lowest frequency mode (mode 7) was calculated against the initial crystal structure. By using the relationship $B=(8\pi^2/3)<R^2>$[53], predicted B-factors of mode 7 were calculated, linearly scaled, and plotted against the observed B-factor from the crystal structure (Fig. 4). Overall, mode 7 exhibited a high correlation with the experimental B-factor. The Pearson correlation coefficient (r) between the predicted and actual B-factor is 0.721. It is an interesting dynamic feature of these low-frequency modes that all the active site resides (Ser189, Glu310, His399) are structurally rigid themselves. In contrast, there are several major flexible regions, including coil_17 and coil_20 (Fig. 7a) in close proximity to the active site gorge. These flexible regions constitute the "excursion" regions E' and F' in α/β fold hydrolase nomenclature [48], and are common features of large esterases. This flexibility near the active site allows the bottom of the gorge to expand and contract, and likely allows the pnbCE to metabolize a variety of substrates with different molecular sizes and chemical properties.

Both modes 7 and 11 represent different characteristic dynamic properties of pnbCE. Mode 7 (Fig. 7a) was

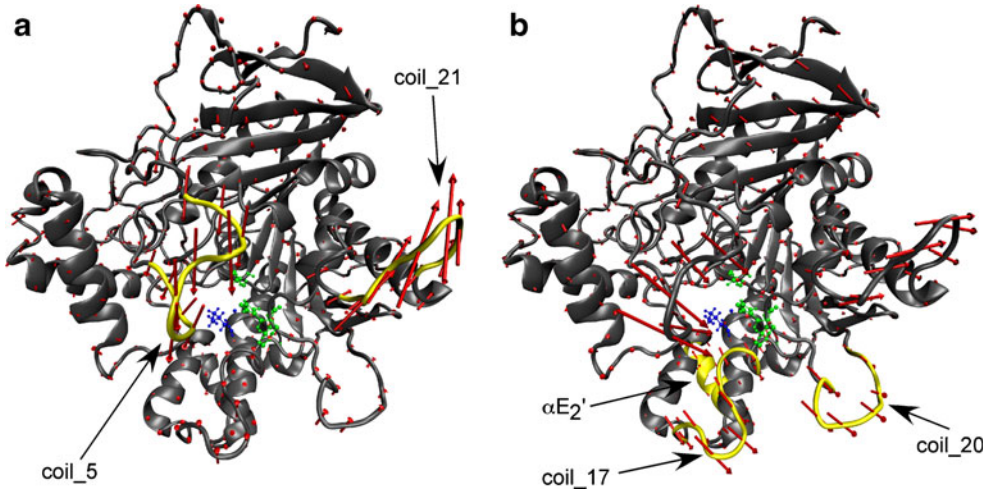

Fig. 7 Normal mode analysis of pnbCE. The ribbon-and-arrow representation of pnbCE, with red arrows indicating the displacements of the C_α atoms. The gray ribbon (backbone) and CPK (active site) representations are shown. The catalytic triad is shown in green, while the "side door" leucine is in blue. The regions of greatest displacement are labeled and indicated by the yellow section. (**a**) Normal mode 7. The yellow section serves as a "lid" over the active site. (**b**) Normal mode 11. Regions in yellow are close to the catalytic triad and contribute to the size change of the catalytic pocket

dominated by motions of two loop regions, coil_5 (residues 61–82) and coil_21 (residues 408–422) that are located on the surface of pnbCE. These two loops were also observed to be flexible in the all-atom MD simulations described above. These motions correspond to the poorly resolved regions (residues 66–74 and 414–420) in the crystal structure, indicating their flexibility. As shown in Fig. 7a, the motions of coil_5 and coil_21 are not only large in magnitude but also highly anti-correlated, while the rest of the protein backbone is essentially rigid. These anti-correlated motions serve to form a flexible cover over the active site, and would necessarily restrict substrate or product entry or exit. The extent of gorge opening and closing at the surface is completely controlled by these loop motions.

On one side of the pnbCE, there is a putative "side door" on the molecular surface, which is directly blocked by Leu362. This "side door" is adjacent to the active site and is 3.0~3.5 Å in diameter, which is similar in size to the narrowest part of the active site gorge diameter. If the "side door" residue unblocks this hole, it could provide a possible entrance for water molecules or exit for small hydrolyzed products. It was indicated in previous studies [14, 16] that this "side door" residue Leu362 plays an essential role during pnbCE-catalyzed hydrolysis of substrates.

In normal mode 7, the putative "side-door" Leu362 is not correlated with the loop motions. However, in normal mode 11 (Fig. 7b), a second major dynamic motion of pnbCE is found. The fluctuation amplitudes of three components, αE_2' (residues 337–346), coil_17 (residues 308–323) and coil_20 (residues 386–401) of pnbCE are enlarged compared to mode 7, indicating a different aspect of dynamic information of pnbCE. In Fig. 7b, it can be seen that these major differences in motions are near the bottom of the active site gorge. αE_2' and coil_17 are situated at the back of the active site behind the "side door" residue Leu362. One of the questions around the "side door" concept is how very large substrates such as CPT-11 could exit via this mechanism following hydrolysis to SN-38. Since αE_2' and coil_17 are located on both sides of Leu362, the anti-correlated motion shown in mode 11 (Fig. 7b) allows these regions to move away from each other, creating a large space at the bottom of the active site gorge that would allow displacement of Leu362 and create a substantial exit route. This is a potential mechanism for opening the "side door" that would be big enough to release large hydrolysis products. Additionally, as part of the active site gorge, this collective motion of coil_17 may contribute significantly to the fluctuation of the gorge size as we saw in our MD simulation.

Normal mode dynamic cross-correlation mapping

The normal modes can also be analyzed with respect to direction by dynamic cross-correlation maps (DCCM) to determine which parts of the molecule behave as units. The DCCM make it straightforward to see how the motion of a single residue is correlated with all other residues in the enzyme. The DCCM of pnbCE for normal mode 7 is shown in Fig. 5a while that for mode 11 is shown in Fig. 5b. A green-red color scale is used to represent the motions, with green indicating correlated motion and red indicating anti-correlated motion. Although, by their very nature, most of the motions calculated by normal mode analysis are correlated to a degree, the DCCM does provide information

about the interconnectivity of the secondary structures and their dynamic relationships, which can be seen as off-diagonal crosspeaks.

The DCCM for normal mode 7 (Fig. 5a) indicates that the predominant correlated segment consists of residues 210–300, which is the region between β-sheet 6 (β6 and α-helix D (αD) of the α/β hydrolase fold. This corresponds to a region containing three α-helices (Fig. 1) and is the common "excursion" location for α/β fold hydrolases (the region where all members of the family are the least homologous [48]). This region is adjacent to the opening of the active site gorge, and is usually the domain that is involved in substrate binding [54]. While the magnitude of the motion in this region is not as large as the surface loop regions (Fig. 4), the DCCM maps indicate that this region acts as an intact, isolated region that evolved to maintain its 3D structure, which would be consistent with a role in substrate binding.

One significant off-diagonal segment consists of the anti-correlated motions between coil_5 and coil_21, as the red arrows indicate in Fig. 7a. Since both loops cover the entrance of the active site gorge, their anti-correlated motions likely play a role in controlling the process of substrate entering or leaving the active site, acting as a lid over the gorge entrance. The other major off-diagonal segment in mode 7 consists of the anti-correlated motions of residues 210–240 and 320–350. As part of the α-helices D and E, they belong to the α/β domain and the regulatory domain, respectively. These α-helices are located at the protein surface around the active site gorge (at the bottom of pnbCE structure in Fig. 7a) and their anti-correlated motions would greatly contribute to the size fluctuation of active site gorge of pnbCE.

The main difference between mode 7 and 11 in DCCM is that mode 7 (Fig. 5a) shows more intact and large scale collective motions, while mode 11 (Fig. 5b) shows more individual secondary structure component motions. This is consistent with mode 11 representing the relatively higher frequency motions comparing with the lowest frequency motions of mode 7. In Fig. 5b, most of the components in the α/β fold domain move in a correlated fashion, including β3, αA, β4, αB, β5, αC, β6, αD and β7. They are the central components of the α/β folding pattern of pnbCE, which carries the catalytic machinery. Thus, these correlated motions are responsible for keeping the structural and functional stability of pnbCE.

Enzyme kinetics of wild-type and mutant pnbCE

Since coil_5 and coil_21 are involved in the lowest-frequency motions within pnbCE by NMA, and since these residues are located at the entrance to the active site, we hypothesized that these anti-correlated motions might be incorporated into the catalytic mechanism of pnbCE. We assessed the effects on catalysis of deleting these loops by using an o-nitrophenyl acetate (o-NPA) hydrolysis kinetics assay (o-NPA is a common substrate for measurement of esterase activity). All three enzymes exhibited standard Michaelis-Menten kinetics (supplemental Fig. 2). As shown in Table 1, minor increases in the K_m value were observed for the Δ[coil_5] and Δ[coil_21] mutant CEs compared to that of the wild-type CE. However, the V_{max} and k_{cat} for the mutant CEs were 4.5-fold and 3-fold smaller than that for the wild-type enzyme, resulting in a 6-fold decrease in the catalytic efficiency (k_{cat}/K_m) of both loop-deleted mutant CEs. These results indicate that, although considerably distant from the active site catalytic residues, the two loops have substantial effects on catalytic activity.

After obtaining these kinetic data, we also conducted a 1 ns MD simulation of pnbCE with its well-characterized substrate para-nitrophenylvalerate (p-NPV) docked into the active site [16]. During the simulation with p-NPV, coil_5 and coil_21 also demonstrated the flexibility observed in the MD simulation of the enzyme alone. However, the substrate does not interact to any extent with these loops, tending instead to closely associate with coil_7 of the enzyme (Fig. 8), which forms part of the oxyanion hole region of the binding site. Taken together, these results suggest that the motions of coil_5 and coil_21 are not part of substrate binding during catalytic turnover, but instead influence ester bond hydrolysis. As discussed below, this is presumably due to prevention of substrate diffusion away from the catalytic active site residues.

Discussion

In this report, we examined the molecular motions inherent in pnbCE, a carboxylesterase from *B. subtilis*. The global structure of pnbCE is that of a α/β fold hydrolase and our analysis was of both low- and high-frequency dynamic motions of individual regions of the enzyme. Our data have important implications for the catalytic mechanism of this family of enzymes.

Recent experimental and computational evidence shows that fast (femtosecond to picosecond) dynamic motions play essential roles in enzymatic transition state barrier crossing [23]. One of the biggest advantages of MD simulation is that it explores the fast dynamic motions at the atomic level, and may provide insight into catalytic mechanisms. In our case, the side chain C-C bond rotation of Glu310 provides a possible mechanism for an on/off switch of the low-barrier hydrogen bond with His399 residue, which is essential in the proposed CE hydrolysis mechanism [51] (Fig. 2). This bond rotation happens fast

Table 1 Kinetic parameters of wt-, Δ[coil_5]-, and Δ[coil_21]- pnbCE using o-NPA as a substrate

Protein	K_m (μM)	V_{max} (μmol min^{-1} mg^{-1})	k_{cat} (s^{-1})	k_{cat}/K_m (s^{-1} mM^{-1})
wt-pnbCE	1705 ± 159	149.9 ± 6.4	135.04	79.20
Δ[coil_5]-pnbCE	2338 ± 363	33.1 ± 2.6	29.82	12.75
Δ[coil_21]-pnbCE	3980 ± 1784	52.1 ± 14.1	46.94	11.79

K_m and V_{max} values are presented as mean±S.E. Previous studies used the extinction coefficient value of 13,600 M^{-1} cm^{-1} [14, 62, 63] for o-NP at 420 nm. When using this value, our K_m and k_{cat} parameters of wt-pnbCE agree with reference value. However, it is reported that 5,220 M^{-1} cm^{-1} is the more accurate extinction coefficient for o-NP [64, 65] and the kinetic parameters in this table are calculated using the new value

enough (200 to 300 ps) to be incorporated into the fast dynamic motions (fs to ps timescale) that link to transition state barrier crossing [23].

Although fast dynamic motions are essential in enzymatic barrier crossing, the overall turnover rate of the enzyme is on the microsecond to millisecond time scale. It is on the same time scale as low-frequency/slow dynamic motions, which usually correspond to loop/domain motions. Our normal mode analysis provides a look at the lowest-frequency, largest structural changes in pnbCE. The loops designated coil_5 and coil_21 form a flexible lid over the entry to the active site gorge. These loops are divergent in the α/β fold hydrolase family and likely help either to control which substrates have access to the active site gorge or which are allowed to exit once the gorge is entered. This can be seen more clearly in Fig. 9, where the views into the active site during the low-frequency motions of normal mode 7 are shown. Mechanistically, our studies suggest molecular details of the enzyme's function. When coil_5 and coil_21 move away from their equilibration conformation, the active site opens and can readily accommodate incoming substrate. Subsequently, the anti-correlated motion of these loops closes the entrance of the gorge and prevents the substrate from diffusing out of the gorge. This model is consistent with our experimental data where deletion of either loop results in mutants that have very similar K_m values to the wild type, but have significantly reduced k_{cat}.

Other details of the catalytic mechanism emerge from our simulations. Once inside the gorge, the fluctuating walls act as a diffusion barrier to substrate access to the catalytic triad. However, the barrier is much smaller in pnbCE as compared to other, more specialized members of the α/β fold hydrolase family since the gorge diameter is much larger. This leads to a greater range of substrates able to arrive at the bottom of the gorge. The enzyme can then release larger products when αE_2', coil_17, and coil_21 move away from the active site in a concerted motion (Fig. 7b) that would create a large gap in the bottom of the active site gorge. These regions then move back into position for hydrolysis of another substrate.

The catalytic residues Ser189, Glu310 and His399 are located at the bottom of the active site gorge comprised of residues 105–108, 193, 215–216, 268–275, 310–314, 362–363, and 399–400 [15]. Coil_5 of pnbCE is located right on top of the active site gorge and, as indicated above in normal mode analysis, is one of the most flexible region of the enzyme. It contains the amino acid sequence PQPSDLLSLSYTELPRQSED between Cys^{61}-Cys^{82} residues, which are predominantly hydrogen bonding and hydrophilic residues. This loop is a characteristic structural element that is conserved among the esterase/lipase family [50]. It is structurally homologous to the large omega loop (Ω loop), Cys^{69}-Cys^{96}, of mouse acetylcholinesterase (mAChE), which was studied extensively by using both

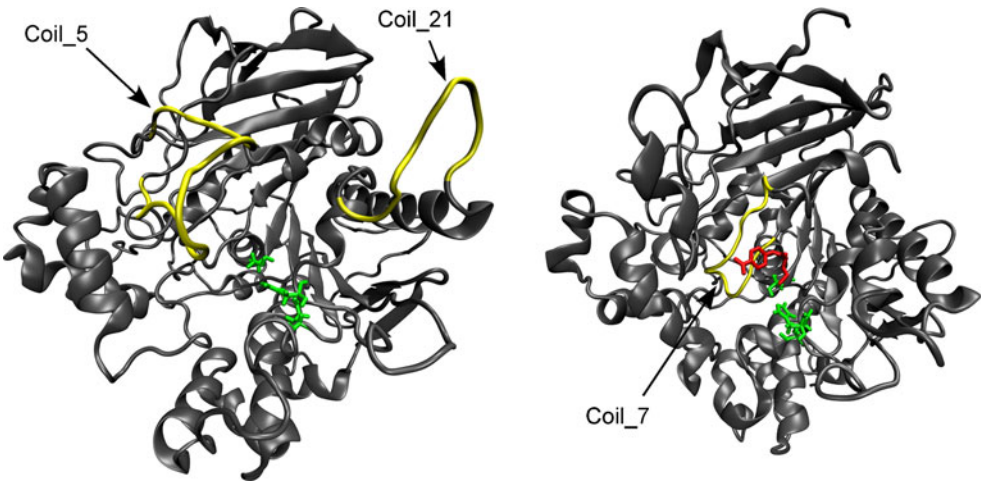

Fig. 8 Substrate binding to pnbCE. The position of p-NPV (red) is shown from the final frame of a 1 ns simulation of the substrate docked into the enzyme active site. The substrate remained in contact with coil_7 throughout the simulation. Also shown are coil_5 and coil_21, indicating their location on the enzyme

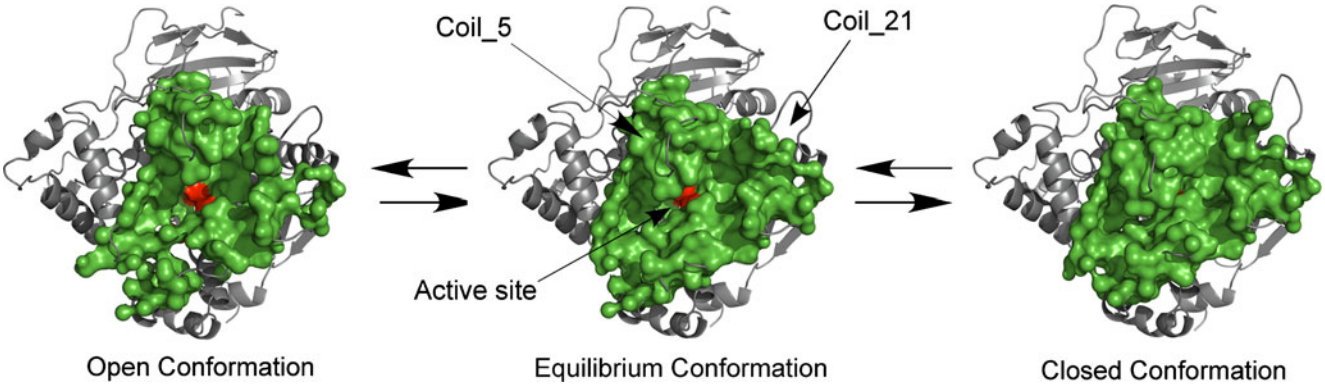

Fig. 9 The solvent accessible surface of pnbCE. The backbone structure is gray and the active site residues are shown in red. The equilibrium crystal structure, open and closed forms are shown from those calculated using normal mode 7. The active site residues are shown in red and the Lee-Richards solvent accessible surface is shown in green. The opening of the active site gorge changes dramatically among all three forms and consequently controls substrate entry and exit from the gorge

computational simulation and experimental measurements [55–57]. It is believed that the conformational change of the Ω loop of AChE plays a crucial role in ligand binding. Among these Ω loop residues, Tyr72 and Asp74, as part of the peripheral anionic site (PAS) of mAChE, bind cationic substrate as the first step in the catalytic pathway [11, 58–60], forming a low-affinity complex at PAS that accelerates catalytic hydrolysis. It is unknown whether the same binding mechanism exists in carboxylesterases, but given the fact that the coil_5 of pnbCE and the Ω loop of mAChE are homologous both sequentially and structurally (sequence alignment below),

```
mAChE     69- CYQYVDTLYPGFEGTEMWNPNRELSEDC -96
                |.|..|.|...:  ||:   .|: ||||
pnbCE     61- CPQPSDLLSLSY--TEL---PRQ-SEDC -82
```

it is likely that this loop plays a similar role in part of the ligand binding process of CEs.

The conformational changes of the Ω loop of mAChE upon ligand binding have been characterized by a combination of cysteine substitution and site-specific labeling experiments [56, 57]. It was concluded from these studies that Ω loop residues are significantly more mobile than other residues around the active site gorge. Our data are consistent with this idea, and we observe coil_5, along with coil_21, being the most flexible structures of pnbCE in both of our normal mode analysis and MD simulation.

Based on our computational and experimental results, our hypothesis is that these loops act as a gate that covers the active site and substrate. These two loops are located on the surface of the enzyme away from the active site. Furthermore, the sequences of these loops are highly variable among members of the α/β hydrolases fold superfamily. Therefore, these loops were not initially expected to be directly involved in the catalytic step of hydrolysis (k_{cat}). However, experimentally they were found to influence k_{cat}. It was recently reported that substituting certain amino acids in the hCE1 loops near the entrance of its active site with the corresponding residues from rCE resulted in an hCE1 variant that has dramatically different kinetic parameters from the wild-type enzyme [61]. Hence, it is not uncommon for some surface loops to be involved in catalysis in this family of enzymes. However, the detailed mechanism that these loops incorporated in the reaction is still unclear. One possible mechanism arising from our dynamics simulations is that these two loops work together and act like a 'lid' that cover the active site gorge. Once the substrate binds near the active site gorge, the lid closes and prevents the substrate from diffusing out of the active site. By removing part of the lid via deletion mutants, this process becomes "leaky" and substrate may diffuse out of the active site and therefore lower the overall rate of catalysis. This 'lid' mechanism would explain the significant decreases of k_{cat} for the loop-deleted mutants compared with wt-pnbCE. This hypothesis provides a direction for additional experimental studies to establish the mechanis-

tic basis of the specific role of each residue on the loop, and these are presently ongoing in our laboratories.

Acknowledgments This work has been supported by the US National Science Foundation EPSCoR grant EPS-0903787, NIH grants CA108775 and P20RR017661, the American Lebanese Syrian Associated Charities (ALSAC), and St. Jude Children's Research Hospital (SJCRH).

References

1. Satoh T, Hosokawa M (1998) The mammalian carboxylesterases: from molecules to function. Annu Rev Pharmacol Toxicol 38:257–288
2. Satoh T, Hosokawa M (2006) Structure, function and regulation of carboxylesterases. Chem Biol Interact 162:195–211
3. Potter PM, Wadkins RM (2006) Carboxylesterases–detoxifying enzymes and targets for drug therapy. Curr Med Chem 13:1045–1054
4. Hicks LD, Hyatt JL, Moak T, Edwards CC, Tsurkan L, Wierdl M, Ferreira A, Wadkins RM, Potter PM (2007) Analysis of the inhibition of mammalian carboxylesterases by novel fluorobenzoins and fluorobenzils. Bioorg Med Chem 15:3801–3817
5. Hicks LD, Hyatt JL, Stoddard S, Tsurkan L, Edwards CC, Wadkins RM, Potter PM (2009) Improved, selective, human intestinal carboxylesterase inhibitors designed to modulate 7-ethyl-10-[4-(1-piperidino)-1-piperidino]carbonyloxycamptothecin (irinotecan; CPT-11) toxicity. J Med Chem 52:3742–3752
6. Hyatt JL, Moak T, Hatfield MJ, Tsurkan L, Edwards C, Wierdl M, Danks MK, Wadkins RM, Potter PM (2007) Selective inhibition of carboxylesterases by isatins, indole-2,3-diones. J Med Chem 50:1876–1885
7. Hyatt JL, Stacy V, Wadkins RM, Yoon KJ, Wierdl M, Edwards CC, Zeller M, Hunter AD, Danks MK, Crundwell G, Potter PM (2005) Inhibition of carboxylesterases by benzil (diphenylethane-1,2-dione) and heterocyclic analogues is dependent upon the aromaticity of the ring and the flexibility of the dione moiety. J Med Chem 48:5543–5550
8. Wadkins RM, Hyatt JL, Edwards CC, Tsurkan L, Redinbo MR, Wheelock CE, Jones PD, Hammock BD, Potter PM (2007) Analysis of mammalian carboxylesterase inhibition by trifluoromethylketone-containing compounds. Mol Pharmacol 71:713–723
9. Wadkins RM, Hyatt JL, Wei X, Yoon KJ, Wierdl M, Edwards CC, Morton CL, Obenauer JC, Damodaran K, Beroza P, Danks MK, Potter PM (2005) Identification and characterization of novel benzil (diphenylethane-1,2-dione) analogues as inhibitors of mammalian carboxylesterases. J Med Chem 48:2906–2915
10. Wadkins RM, Hyatt JL, Yoon KJP, Morton CL, Lee RE, Damodaran K, Beroza P, Danks MK, Potter PM (2004) Discovery of novel selective inhibitors of human intestinal carboxylesterase for the amelioration of irinotecan-induced diarrhea: synthesis, quantitative structure-activity relationship analysis, and biological activity. Mol Pharmacol 65:1336–1343
11. Wadkins RM, Morton CL, Weeks JK, Oliver L, Wierdl M, Danks MK, Potter PM (2001) Structural constraints affect the metabolism of 7-ethyl-10-[4-(1-piperidino)-1-piperidino]carbonyloxycamptothecin (CPT-11) by carboxylesterases. Mol Pharmacol 60:355–362
12. Nagel ZD, Klinman JP (2009) A 21st century revisionist's view at a turning point in enzymology. Nature Chem Biol 5:543–550
13. Hatfield JM, Wierdl M, Wadkins RM, Potter PM (2008) Modifications of human carboxylesterase for improved prodrug activation. Expert Opin Drug Metab Toxicol 4:1153–1165
14. Wierdl M, Morton CL, Nguyen NK, Redinbo MR, Potter PM (2004) Molecular modeling of CPT-11 metabolism by carboxylesterases (CEs): use of pnb CE as a model. Biochemistry 43:1874–1882
15. Spiller B, Gershenson A, Arnold FH, Stevens RC (1999) A structural view of evolutionary divergence. Proc Natl Acad Sci USA 96:12305–12310
16. Streit TM, Borazjani A, Lentz SE, Wierdl M, Potter PM, Gwaltney SR, Ross MK (2008) Evaluation of the 'side door' in carboxylesterase-mediated catalysis and inhibition. Biol Chem 389:149–162
17. Lushington GH, Guo J-X, Hurley MM (2006) Acetylcholinesterase: molecular modeling with the whole toolkit. Curr Top Med Chem 6:57–73
18. Kua J, Zhang Y, McCammon JA (2002) Studying enzyme binding specificity in acetylcholinesterase using a combined molecular dynamics and multiple docking approach. J Am Chem Soc 124:8260–8267
19. Shen T, Tai K, Henchman RH, McCammon JA (2002) Molecular dynamics of acetylcholinesterase. Acc Chem Res 35:332–340
20. Wintrode PL, Zhang D, Vaidehi N, Arnold FH, Goddard WA III (2003) Protein Dynamics in a Family of Laboratory Evolved Thermophilic Enzymes. J Mol Biol 327:745–757
21. Vistoli G, Pedretti A, Mazzolari A, Testa B (2010) In silico prediction of human carboxylesterase-1 (hCES1) metabolism combining docking analyses and MD simulations. Bioorg Med Chem 18:320–329
22. Hammes-Schiffer S, Benkovic SJ (2006) Relating protein motion to catalysis. Annu Rev Biochem 75:519–541
23. Schwartz SD, Schramm VL (2009) Enzymatic transition states and dynamic motion in barrier crossing. Nat Chem Biol 5:551–558
24. Case DA, Darden TA, Cheatham TE, Simmerling CL, Wang J, Duke RE, Luo R, Merz KM, Wang B, Pearlman DA, Crowley M, Brozell S, Tsui V, Gohlke H, Mongan J, Hornak V, Cui G, Beroza P, Schafmeister C, Caldwell JW, Ross WS, Kollman PA (2004) AMBER 8. University of California, San Francisco
25. Suhre K, Sanejouand YH (2004) ElNemo: a normal mode web server for protein movement analysis and the generation of templates for molecular replacement. Nucleic Acids Res 32(Web Server issue):W610–614
26. Amaro RE, Minh DD, Cheng LS, Lindstrom WM Jr, Olson AJ, Lin JH, Li WW, McCammon JA (2007) Remarkable loop flexibility in avian influenza N1 and its implications for antiviral drug design. J Am Chem Soc 129:7764–7765
27. Baron R, McCammon JA (2007) Dynamics, hydration, and motional averaging of a loop-gated artificial protein cavity: the W191G mutant of cytochrome c peroxidase in water as revealed by molecular dynamics simulations. Biochemistry 46:10629–10642
28. Amaro RE, Cheng X, Ivanov I, Xu D, McCammon JA (2009) Characterizing loop dynamics and ligand recognition in human- and avian-type influenza neuraminidases via generalized born molecular dynamics and end-point free energy calculations. J Am Chem Soc 131:4702–4709
29. Sali A, Blundell TL (1993) Comparative Protein Modelling by Satisfaction of Spatial Restraints. J Mol Biol 234:779–815
30. Pearlman DA, Case DA, Caldwell JW, Ross WS, Cheatham TE III, DeBolt S, Ferguson D, Seibel G, Kollman P (1995) AMBER, a package of computer programs for applying molecular mechanics, normal mode analysis, molecular dynamics and free energy calculations to simulate the structural and energetic properties of molecules. Comput Phys Commun 91:1–41
31. Frishman D, Argos P (1995) Knowledge-based protein secondary structure assignment. Proteins 23:566–579
32. Cornell WD, Cieplak P, Bayly CI, Gould IR, Merz KMJ, Ferguson DM, Spellmeyer DC, Fox T, Caldwell JW, Kollman

PA (1995) A second generation force field for the simulation of proteins and nucleic acids. J Am Chem Soc 117:5179–5197
33. Hawkins GD, Cramer CJ, Truhlar DG (1996) Parametrized models of aqueous free energies of solvation based on pairwise descreening of solute atomic charges from a dielectric medium. J Phys Chem 100:19824–19839
34. Morishita T (2000) Fluctuation formulas in molecular-dynamics simulations with the weak coupling heat bath. J Chem Phys 113:2976–2982
35. Ryckaert J-P, Ciccotti G, Berendsen HJC (1977) Numerical integration of the cartesian equations of motion of a system with constraints: molecular dynamics of n-alkanes. J Comput Phys 23:327–341
36. Hinsen K (2000) The molecular modeling toolkit: a new approach to molecular simulations. J Comput Chem 21:79–85
37. Tara S, Helms V, Straatsma TP, McCammon JA (1999) Molecular dynamics of mouse acetylcholinesterase complexed with huperizine A. Biopolymers 50:347–359
38. Morris GM, Goodsell DS, Halliday RS, Huey R, Hart WE, Belew RK, Olson AJ (1998) Automated docking using a Lamarckian genetic algorithm and an empirical binding free energy function. J Comput Chem 19:1639–1662
39. Wang J, Cieplak P, Kollman PA (2000) How well does a restrained electrostatic potential (RESP) model perform in calculating conformational energies of organic and biological molecules? J Comput Chem 21:1049–1074
40. Wang J, Wolf RM, Caldwell JW, Kollman PA, Case DA (2004) Development and testing of a general Amber force field. J Comput Chem 25:1157–1174
41. Srinivasan J, Cheatham TEI, Cieplak P, Kollman P, Case DA (1998) Continuum solvent studies of the stability of DNA, RNA, and phosphoramidite-DNA helices. J Am Chem Soc 120:9401–9409
42. Tama F, Gadea FX, Marques O, Sanejouand YH (2000) Building-block approach for determining low-frequency normal modes of macromolecules. Protein Struct Funct Gen 41:1–7
43. Dundas J, Ouyang Z, Tseng J, Binkowski A, Turpaz Y, Liang J (2006) CASTp: computed atlas of surface topography of proteins with structural and topographical mapping of functionally annotated residues. Nucleic Acids Res 34(Web Server issue):W116–118
44. Edelsbrunner H, Facello M, Liang J (1998) On the definition and the construction of pockets in macromolecules. Discrete Appl Math 88:83–102
45. Lee B, Richards FM (1971) The interpretation of protein structures: estimation of static accessibility. J Mol Biol 55:379–400
46. Connolly ML (1983) Analytical Molecular-Surface Calculation. J Appl Crystallogr 16:548–558
47. Reyes-Duarte D, Polaina J, Lopez-Cortes N, Alcalde M, Plou FJ, Elborough K, Ballesteros A, Timmis KN, Golyshin PN, Ferrer M (2005) Conversion of a carboxylesterase into a triacylglycerol lipase by a random mutation. Angew Chem Int Edn Engl 44:7553–7557
48. Ollis DL, Cheah E, Cygler M, Dijkstra B, Frolow F, Franken SM, Harel M, Remington SJ, Silman I, Schrag J, Sussman JL, Verschueren KHG, Goldman A (1992) The α/β hydrolase fold. Prot Eng 5:197–211
49. Bencharit S, Morton CL, Hyatt JL, Kuhn P, Danks MK, Potter PM, Redinbo MR (2003) Crystal structure of the human carboxylesterase 1 complexed with the Alzheimer's drug tachrine: from binding promiscuity to selective inhibition. Chem Biol 10:341–349
50. Cygler M, Schrag JD, Sussman JL, Harel M, Silman I, Gentry MK, Doctor BP (1993) Relationship between sequence conservation and three-dimensional structure in a large family of esterases, lipases, and related proteins. Protein Sci 2:366–382
51. Frey PA, Whitt SA, Tobin JB (1994) A low-barrier hydrogen bond in the catalytic triad of serine proteases. Science 264:1927–1930
52. Tama F (2003) Normal mode analysis with simplified models to investigate the global dynamics of systems. Protein Pept Lett 10:119–132
53. McCammon JA, Harvey SC (1987) Dynamics of proteins and nucleic acids. Cambridge University Press, New York
54. Heikinheimo P, Goldman A, Jeffries C, Ollis DL (1999) Of barn owls and bankers: a lush variety of α/β hydrolases. Structure 7: R141–R146
55. Tai K, Shen T, Börjesson U, Philippopopoulos M, McCammon JA (2001) Analysis of a 10-nanosecond molecular dynamics simulation of mouse acetylcholinesterase. Biophys J 81:715–724
56. Shi JX, Boyd AE, Radic Z, Taylor P (2001) Reversibly bound and covalently attached ligands induce conformational changes in the omega loop, Cys(69)-Cys(96), of mouse acetylcholinesterase. J Biol Chem 276:42196–42204
57. Shi J, Tai K, McCammon JA, Taylor P, Johnson DA (2003) Nanosecond dynamics of the mouse acetylcholinesterase Cys69-Cys96 omega loop. J Biol Chem 278:30905–30911
58. Hosea NA, Radic Z, Tsigelny I, Berman HA, Quinn DM, Taylor P (1996) Aspartate 74 as a primary determinant in acetylcholinesterase governing specificity to cationic organophosphonates. Biochemistry 35:10995–11004
59. Szegletes T, Mallender WD, Thomas PJ, Rosenberry TL (1999) Substrate binding to the peripheral site of acetylcholinesterase initiates enzymatic catalysis. Substrate inhibition arises as a secondary effect. Biochemistry 38:122–133
60. Mallender WD, Szegletes T, Rosenberry TL (2000) Acetylthiocholine binds to asp74 at the peripheral site of human acetylcholinesterase as the first step in the catalytic pathway. Biochemistry 39:7753–7763
61. Wierdl M, Tsurkan L, Hyatt JL, Edwards CC, Hatfield MJ, Morton CL, Houghton PJ, Danks MK, Redinbo MR, Potter PM (2008) An improved human carboxylesterase for enzyme/prodrug therapy with CPT-11. Cancer Gene Ther 15:183–192
62. Hatfield MJ, Tsurkan L, Hyatt JL, Yu X, Edwards CC, Hicks LD, Wadkins RM, Potter PM (2010) Biochemical and molecular analysis of carboxylesterase-mediated hydrolysis of cocaine and heroin. Br J Pharmacol 160:1916–1928
63. Danks MK, Morton CL, Pawlik CA, Potter PM (1998) Overexpression of a rabbit liver carboxylesterase sensitizes human tumor cells to CPT-11. Cancer Res 58:20–22
64. Soundararajan M, Bailey CP, Markwell J (2008) Use of a laboratory exercise on molar absorptivity to help students understand the authority of the primary literature. Biochem Mol Biol Edu 36:61–64
65. Láng LJS, Varsányi G, Vizesy M (1961) Absorption spectra in the ultraviolet and visible region. In: A theoretical and technical introduction, vol 1. Academic, New York, p 413